ADVANCED MATERIALS

Supporting Information

A Novel Soft-Magnetic B2-Based Multiprincipal-Element Alloy with a Uniform Distribution of Coherent Body-Centered-Cubic Nanoprecipitates

Yue Ma, Qing Wang,* Xuyang Zhou, Jiamiao Hao, Baptiste Gault, Qingyu Zhang, Chuang Dong, and T. G. Nieh*

Supporting Information

A Novel Soft-Magnetic B2-Based Multi-Principal-Element Alloy with a Uniform Distribution of Coherent Body-Centered-Cubic Nanoprecipitates

Yue Ma[1], Qing Wang,[1],* Xuyang Zhou[2], Jiamiao Hao[1], Baptiste Gault[2,3], Qingyu Zhang[4], Chuang Dong[1], T.G. Nieh[5],*

[1] Key Laboratory of Materials Modification by Laser, Ion and Electron Beams (Ministry of Education), School of Materials Science and Engineering, Dalian University of Technology, Dalian 116024, China
[2] Max-Planck-Institut für Eisenforschung, Max-Planck-Straße 1, Düsseldorf 40237, Germany
[3] Department of Materials, Royal School of Mines, Imperial College, London, SW7 2AZ, United Kingdom
[4] School of Physics, Dalian University of Technology, Dalian 116024, China
[5] Department of Materials Science and Engineering, University of Tennessee, Knoxville, Tennessee 37996, USA
E-mail addresses: wangq@dlut.edu.cn (Q. Wang), tnieh@utk.edu (T. G. Nieh)

Sample preparation

The designed $Al_{1.5}Co_4Fe_2Cr$ ($Al_{17.65}Co_{47.06}Fe_{23.53}Cr_{11.76}$, at. %) alloy was prepared by means of arc melting and suction cast into a copper mold with dimension of 2 mm-thick and 9 mm-wide plates under an argon atmosphere. Purities of the raw metals are 99.99 % for Al, Co, and Fe, and 99.9 % for Cr. Mixtures of raw materials with the nominal composition and a total weight of about 6 g were remelted at least five times to obtain high-quality specimens. These as-cast $Al_{1.5}Co_4Fe_2Cr$ alloy plates were homogenized at 1573 K for 2 h, and then aged at 773 K, 873 K, 973 K, and 1073 K for 24 h, designated as A-773, A-873, A-973, and A-1073, respectively. In addition, the A-773 specimens were also heat-treated at 873 K for different times of 8 h, 70 h, 305 h and 555 h, in order to study the thermal stability of the soft-magnetic properties. Each treatment was followed by water-quenching.

Calculation of lattice misfit

The lattice misfit between the BCC and B2 phases in A-773 alloy was calculated according to the formula of $\varepsilon = 2 \times (a_{B2} - a_{BCC})/(a_{B2} + a_{BCC})$,[S1] in which a_{B2} and a_{BCC} are the lattice constants of B2 and BCC phases, respectively. In addition, the crystal structure of A-773 was identified using a Bruker D8 X-ray diffractometer (XRD) with the Cu K_α radiation ($\lambda = 0.15406$ nm), and the external standard method was applied to calculate the lattice constants.[S2]

APT analysis

The chemical information was investigated using atom probe tomography (APT) at the near-atomic scale. The required needle-shaped geometry for APT specimens was prepared using a focus ion beam (FIB) lift-out and annular milling technique in a FEI Helios Nanolab 600i.[S3] The specimens were field analyzed in a Cameca Instruments Local Electrode Atom Probe (LEAP) 5000 HR operated at a specimen setpoint temperature of 50 K and laser pulse energy of 5 pJ at a pulse repetition rate of 200 kHz for a 0.5 % atoms per pulse detection rate. The APT data were reconstructed using the IVAS 3.8.4 software platform, and the reconstruction has been calibrated based on the methodology described in Ref. [S4]. In Figure 1f, we overlaid sets

of 35 at. % Cr and 33 at. % Fe iso-composition surfaces on top of the point cloud to highlight the elemental distributions around Cr clusters.

Statistics on particle size of nanoprecipitates

Image analysis of the microstructural details were made in the ImageJ software.[S5] Statistical analysis on the size of BCC precipitated particles was performed with at least 6 TEM morphology images. The particle size was obtained from over 150 particles, and defined using an area-equivalent diameter (*i.e.*, $r = 2 \times \sqrt{area/\pi}$). In addition, the standard error (*SE*) in *r* was obtained using $SE = \sigma/\sqrt{N}$, where σ is the standard deviation of particle sizes, and *N* is the number of precipitates.

Calculation of the mean magnetic moment per atom $\overline{\mu}_H$

The saturation induction intension B_S depends on the content in the ferromagnetic elements of Fe, Co and Ni.[S6] If we consider only the change in ferromagnetic element content, the mean magnetic moment per atom $\overline{\mu}_H$ can be expressed as

$$\overline{\mu}_H = \sum \mu_{H,i} \cdot x_i \qquad \text{(S1)}$$

where $\mu_{H,i}$ is the experimental magnetic moment per atom, *i.e.*, $\mu_{H,Fe}$=2.2μ_B, $\mu_{H,Co}$=1.7μ_B, and $\mu_{H,Ni}$ =0.6μ_B (μ_B, Bohr magneton),[S6] and x_i is the atomic concentration of Fe, Co, and Ni elements.

The Cluster formula approach for Composition Design

In our previous work, we proposed a 'cluster-plus-glue-atom' structural model to describe the local atomic distribution of alloying elements based on the chemical short-range orders (CSROs).[S7-S10] The CSROs are the most typical structural characteristics of solid solutions due to the obvious local structural heterogeneities with respect to the average crystal structure, which plays an important role to the diverse mechanical and physical properties of alloys.[S11-S15] In this cluster model, the cluster is the nearest-neighbor polyhedron centered by a solute atom who has the strong interaction with the base solvent atoms to represent the strongest

CSRO. Some other solute atoms (i.e., glue atoms) with weak interactions are certainly required to fill the space between the clusters to balance the atomic-packing density. Thus, a uniform composition formula [cluster](glue atom)$_x$ (x being the glue atom number) can be obtained from the cluster model, named the cluster formula approach.[S7-S9] The sites of the solute elements in the cluster formula is determined according to the enthalpy of the mixing (ΔH) between the solute and the base element that represents the interaction between them.[S16] That is to say, the solute element having a large negative ΔH with the base preferentially occupies the cluster center site to form a stable cluster, while that with a positive ΔH tends to occupy the glue atom site. Besides, the cluster-shell sites are primarily occupied by the base solvent atoms, as well as some solutes having a zero ΔH with the base. So the cluster formula [cluster](glue atom)$_x$, containing all the key information on the alloy chemistry, i.e., chemical compositions, atomic occupancies (at the center, shell and glue sites) and chemical bonds in a cluster structural unit, can be regarded as the molecular formula for alloy structure. Particularly, in the BCC structure, the nearest-neighbor cluster is the rhombi-dodecahedron with a coordination number (CN) of 14 (the 1st-shell CN8 + 2nd-shell CN6), and the glue atom number x was ideally calculated as x = 1, 2, or 3.[S8] Since the multi-principal-element alloys (MPEAs), also named the high entropy alloys (HEAs), can be treated as a special kind of solid solution alloys, CSROs have been confirmed in some HEAs by both neutron scattering experiments and simulations.[S17, S18] Thus, we applied the cluster formula approach into the HEA-forming systems for composition design to tailor their microstructures.[S19]

For instance, we used a cluster formula of [Al-M$_{14}$]Al$_1$ (M represents different combinations of Co, Cr, Fe, and Ni) to design a series of Al-Co-Cr-Fe-Ni HEAs, which exhibit special coherent microstructure with ordered B2 nanoprecipitates dispersed into the BCC solid solution matrix.[S10, S19, S20] Especially, the precipitation of cuboidal B2 nanoparticles in the BCC matrix render these HEAs with higher yield strength (1.7 ~ 2.2 GPa) and better microstructural stability at high temperatures.[S20] In addition, the B2 nanoprecipitates are enriched by Al and Ni, while

Fe, Co and Cr are segregated preferentially in the BCC matrix.[S19] The cluster formula of the current $Al_{1.5}Co_4Fe_2Cr$ alloy will be described in the following section.

Design strategy of soft-magnetic alloys with coherent nanoprecipitates

The magnetic property of materials is closely related to the magnetic domains, in which the internal stress induced by crystalline defects can block the movement of domain walls in an applied magnetic field, resulting in an increase in the total energy of system.[S21-S23] When the domain wall moves to a certain position of x, the domain wall energy E_w will increase, but the magnetostatic energy E_H will decrease in order to achieve the energy minimum. In other words, E_H and E_w offset each other and we have Equation S2:[S21-S23]

$$\frac{\partial E_H}{\partial x} + \frac{\partial E_w}{\partial x} = 0 \tag{S2}$$

$$E_H = -2\mu_0 H_C M_S x \cos\theta \tag{S2a}$$

$$E_w = 2\sqrt{A/\left[K_1 + \frac{3}{2}\lambda_s \sigma(x)\right]} = 2 \cdot \delta \tag{S2b}$$

where μ_0 is the permeability of vacuum, θ is the angle between the magnetic moment and the magnetic field direction after the movement of domain wall, A is a constant, K_1 is the magnetic anisotropy constant, λ_s is the magnetostriction coefficient, $\sigma(x)$ is the internal stress field caused by the various crystalline defects (especially the boundaries of grains and ultrafine precipitates) that is related to the position x, and δ is the width of the domain wall.[S21-S23] Apparently, the coercivity H_C is associated to the internal stress $\sigma(x)$. Since the $\sigma(x)$ is a wave function with a characteristic wavelength l, the coercivity H_C could be calculated through Equation S3: [S21-S23]

$$H_C = \frac{\lambda_s \Delta\sigma}{2\mu_0 M_S \cos\theta} \frac{3\delta/l}{1+3(\delta/l)^2} \tag{S3}$$

where $\Delta\sigma$ is the amplitude of internal stress wave. Thus, the coercivity H_C depends on a series of parameters, λ_s, M_S, θ, δ, and l. Especially, the characteristic wavelength l is crucial for achieving a low H_C since it is related to the grain size D_g of materials that could be tuned through material processing. For instance, when the l is much larger than the width of domain wall δ (i.e., $l >> \delta$), the coercivity H_C of Mn-Zn soft ferrite could reach a minimum of $H_C = 6.4$ A/m at a grain size $D_g > 5$ μm, in which the ratio of δ / l is dominant.[S21] On the other extreme, if the l is effectively reduced such that $l << \delta$, like in materials containing ultrafine ferromagnetic nanoprecipitates, a low H_C could also be obtained in light of Equation S3 due to the dominant term of $(\delta / l)^2$.

From Equation S3, it can be seen that a low H_C can also be obtained by increasing the saturation magnetization M_S, which can be obtained in BCC structure rather than FCC. For example, it has been demonstrated that magnetic exchange interactions from nearest-neighbor atomic pairs of Fe-Fe, Fe-Co, and Co-Co could give the maximum contribution to a high M_S in Fe-Co-Cr-Ni-Al HEAs, and these interactions in the BCC structure are stronger than those in the FCC due to different chemical short-range orders (CSROs).[S24] In addition, the effects of λ_s and θ on H_C could be negligible, except in the presence of oriented texture.[S23] Therefore, it is possible to obtain high-performance soft-magnetic alloys through tuning the microstructure to contain ultrafine BCC ferromagnetic nanoprecipitates in a B2 matrix.

However, to get a special coherent microstructure with ultrafine BCC ferromagnetic nanoprecipitates in a B2 matrix is still challenging since it is susceptible to the compositional difference between BCC and B2 phases. A weave-like or plate-like spinodal decomposition microstructure of BCC and B2 was always observed in these HEAs due to a large composition difference between them.[S25-S28] Intensive efforts have been made to explore the possibility to precipitate spherical or cuboidal particles in a large variety of BCC-related alloy systems through adjusting the concentrations of both Al and transition metals.[S19, S20, S29-S31] It is known

that the main driving force for the growth of coherent particles is the elastic energy, which is determined by the lattice misfit strain, ε, between the precipitated phase and the matrix.[S32-S35] Small spherical nanoprecipitates are generally observed at a relatively small ε (< 0.2 %) in Al-Ni-Co-Fe-Cr HEAs.[S19] Thus, it is necessary to deliberately tune the compositions of BCC and B2 phases simultaneously to minimize the ε in order to achieve a unique coherent microstructure which has a uniform distribution of ferromagnetic BCC nanoprecipitates in the B2 matrix.

Among the ferromagnetic elements Fe, Co, and Ni, the magnetic moment μ_H of Ni is much less than that of Fe or Co ($\mu_{H,Fe}$ = 2.2μ_B, $\mu_{H,Co}$ = 1.7μ_B, and $\mu_{H,Ni}$ = 0.6μ_B.).[S6] Therefore, to maximize the magnetic moment and the saturation magnetization M_S, Ni should be removed to ensure that the BCC nanoprecipitate is enriched with more Co and Fe. The Al element is crucial to form the FeAl and CoAl B2 phases in Al-Co-Fe-Cr system.[S36] And the content of Al must higher than that in previous [Al-M_{14}]Al$_1$ alloys in order to realize the phase inversion, i.e., the BCC nanoparticles are precipitated in the B2 matrix. Therefore, another cluster formula with the glue atom number of $x = 2$ will be applied in the present work to design alloy compositions of [Al-M_{14}]Al$_2$. Another important note is that BCC and B2 often form a weave-like microstructure, instead of a desirable particle precipitation in Co-Fe-Ni-Al-based magnetic alloys.[S37] This feature has been attributed to a larger lattice misfit ε caused by a large compositional difference between BCC and B2. In order to minimize the lattice misfit for bypassing the formation of weave-like microstructure, Cr was introduced to reduce the lattice misfit for producing spherical nanoprecipitates. Taken into account of all these considerations, M in the cluster formula is composed of Co, Fe, and Cr, in which Co occupies preferentially the 1st-shell sites with CN8 due to the relatively-strong interactions with Al ($\Delta H_{Al\text{-}Co}$ = -19 kJ·mol^{-1}),[S16] and Fe and Cr occupies the 2nd-shell sites of CN6 ($\Delta H_{Al\text{-}Fe}$ = -11 kJ·mol^{-1}, and $\Delta H_{Al\text{-}Cr}$ = -10 kJ·mol^{-1})[S16] with a ratio of Fe/Cr = 2/1 due to the ferromagnetism of Fe.

Accounting for all these considerations, the [Al-(Co$_8$Fe$_4$Cr$_2$)]Al$_2$ cluster formula (Al$_{1.5}$Co$_4$Fe$_2$Cr, Al$_{17.65}$Co$_{47.06}$Fe$_{23.53}$Cr$_{11.76}$, at. %) was finally designed to obtain the coherent microstructure with BCC nanoprecipitates (Fe, Co, and Cr-rich) in the B2 matrix (Al and Co-rich).
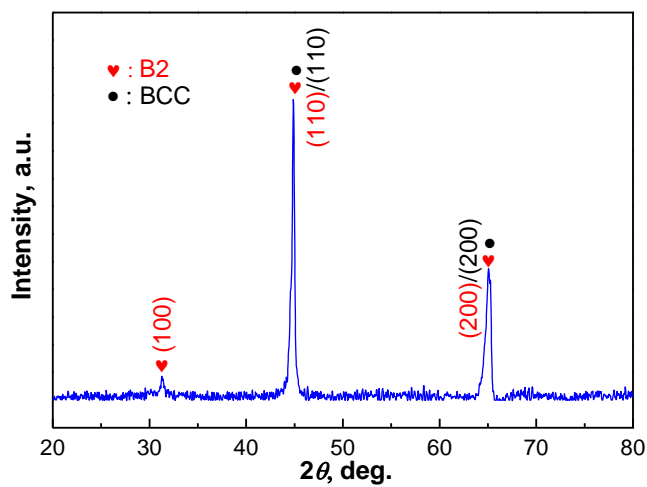
Figure S1. XRD pattern of the $Al_{1.5}Co_4Fe_2Cr$ alloy after aging at 773 K for 24 h (A-773), consisting of BCC and B2 phases. The lattice constants of these two phases are $a_{BCC} = 0.2897$ nm and $a_{B2} = 0.2900$ nm, respectively.
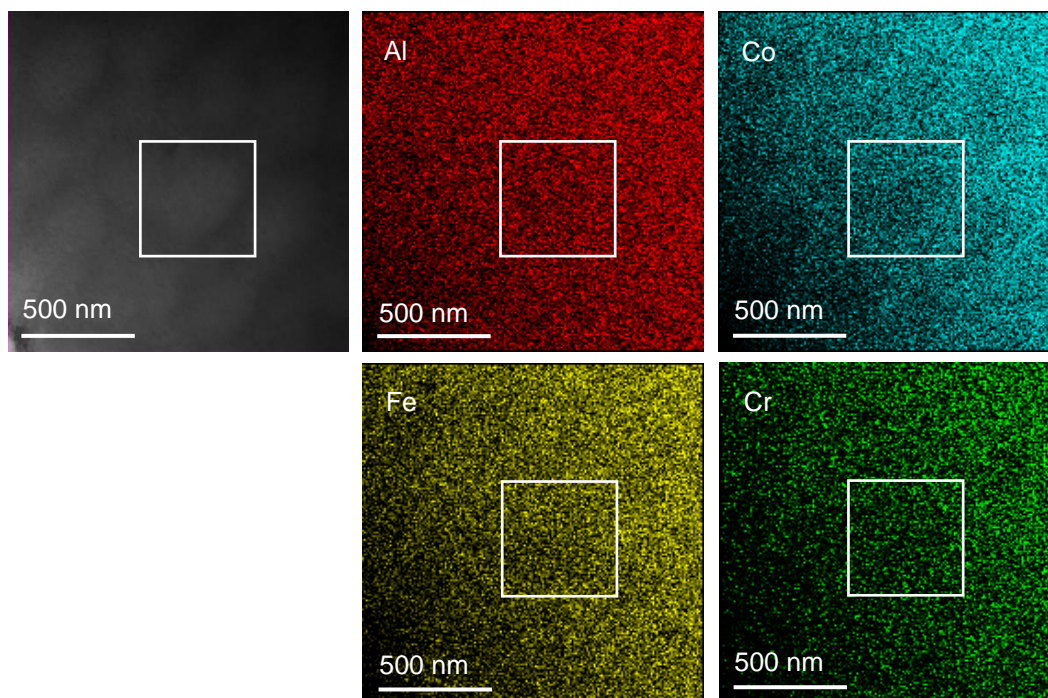
Figure S2. Elemental distribution in the micron-structure of the A-773 alloy mapped with STEM, in which the micron-scaled cell boundaries are slightly enriched with Co and Cr elements.
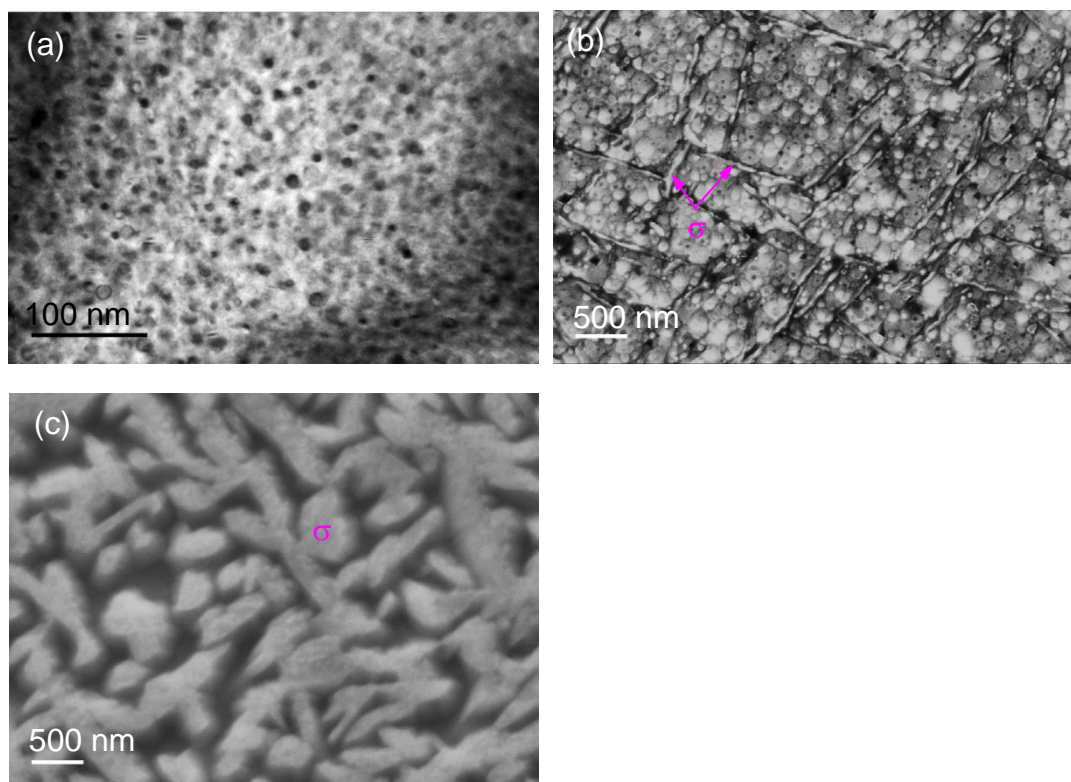
Figure S3. (a) TEM bright-field (BF) image of the A-873 specimen, (b) SEM image of the A-973 specimen, (c) SEM image of the A-1073 specimen.
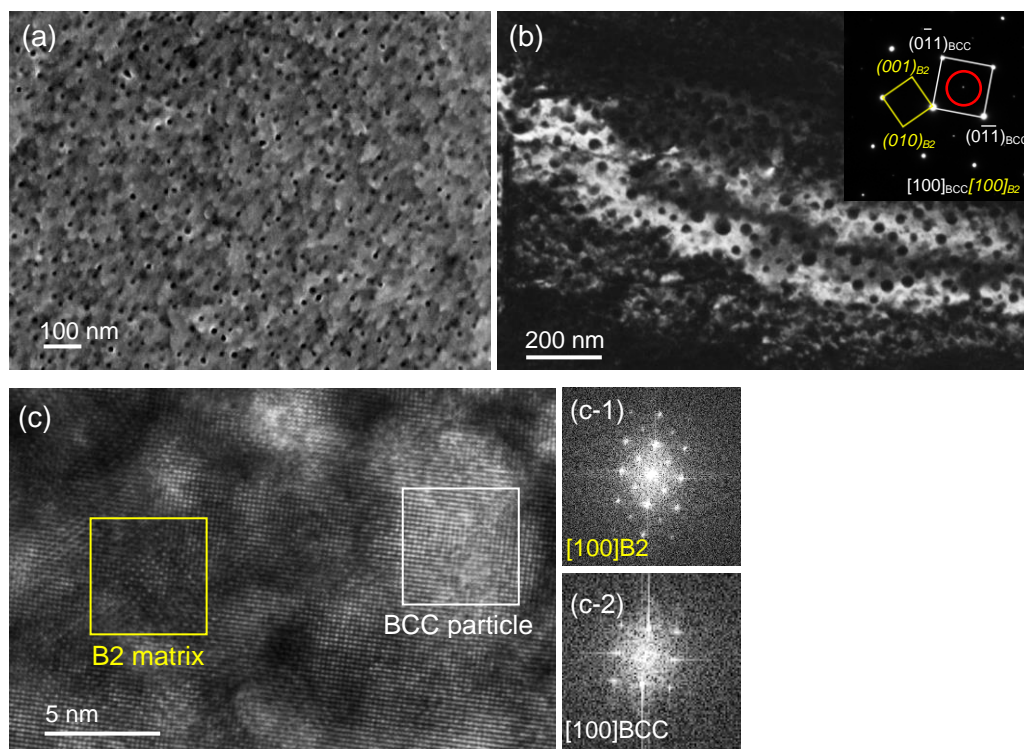
Figure S4. SEM and TEM images of 555 h-aged specimen at 873 K. (a) SEM image; (b) TEM-DF image and the corresponding SEAD pattern, showing that the uniform BCC particles are coherently embedded in B2 matrix; (c) HRTEM image of B2 matrix and BCC particle, in which the FFT patterns obtained from the B2 matrix (c-1) and BCC particle (c-2) are also given.
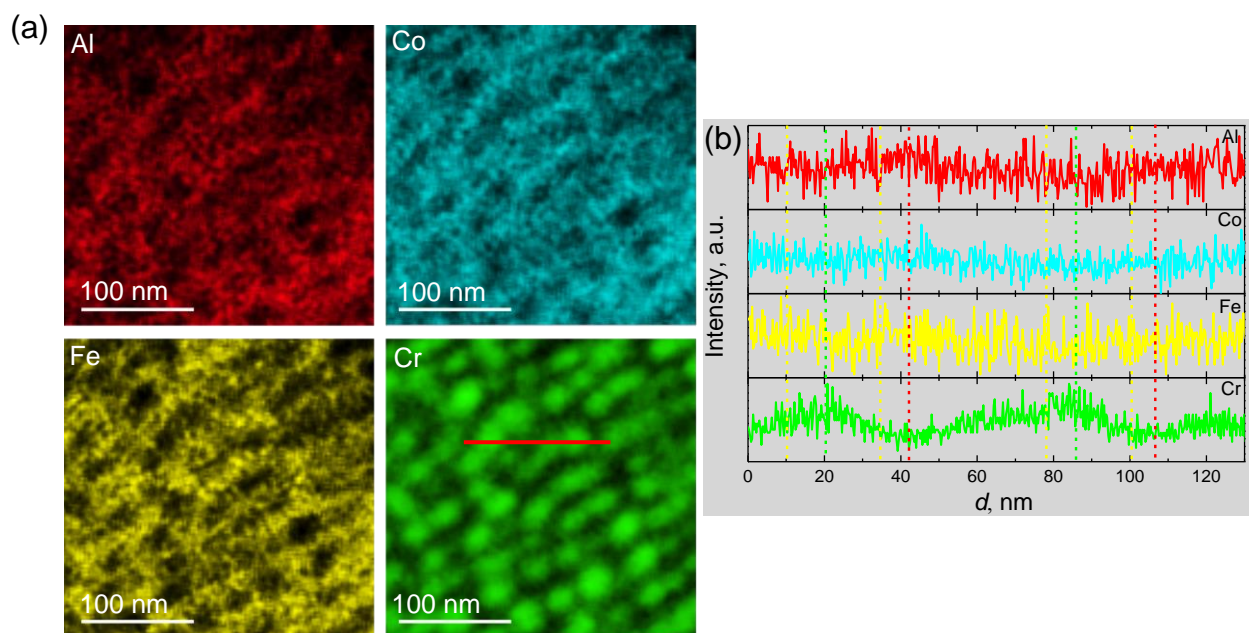
Figure S5. Elemental distributions in 873 K-aged specimen for 555 h obtained with the FIB-EDS. (a) Elemental mapping, showing that the BCC nanoparticles are enriched with Cr and the B2 matrix is enriched with Al and Co; (b) Linear-scanning analysis from the red line in (a), indicating that Fe is enriched around the Cr-cores to form core-shell strucutred BCC nanoparticles, rather than enriched in the B2 matrix alone, as evidenced by the yellow and green dotted lines. Obviously, the Al-rich regions (marked with red dotted lines) correspond to the Cr-poor regions. The basic Co element is uniformly distributed in the Cr-poor regions.
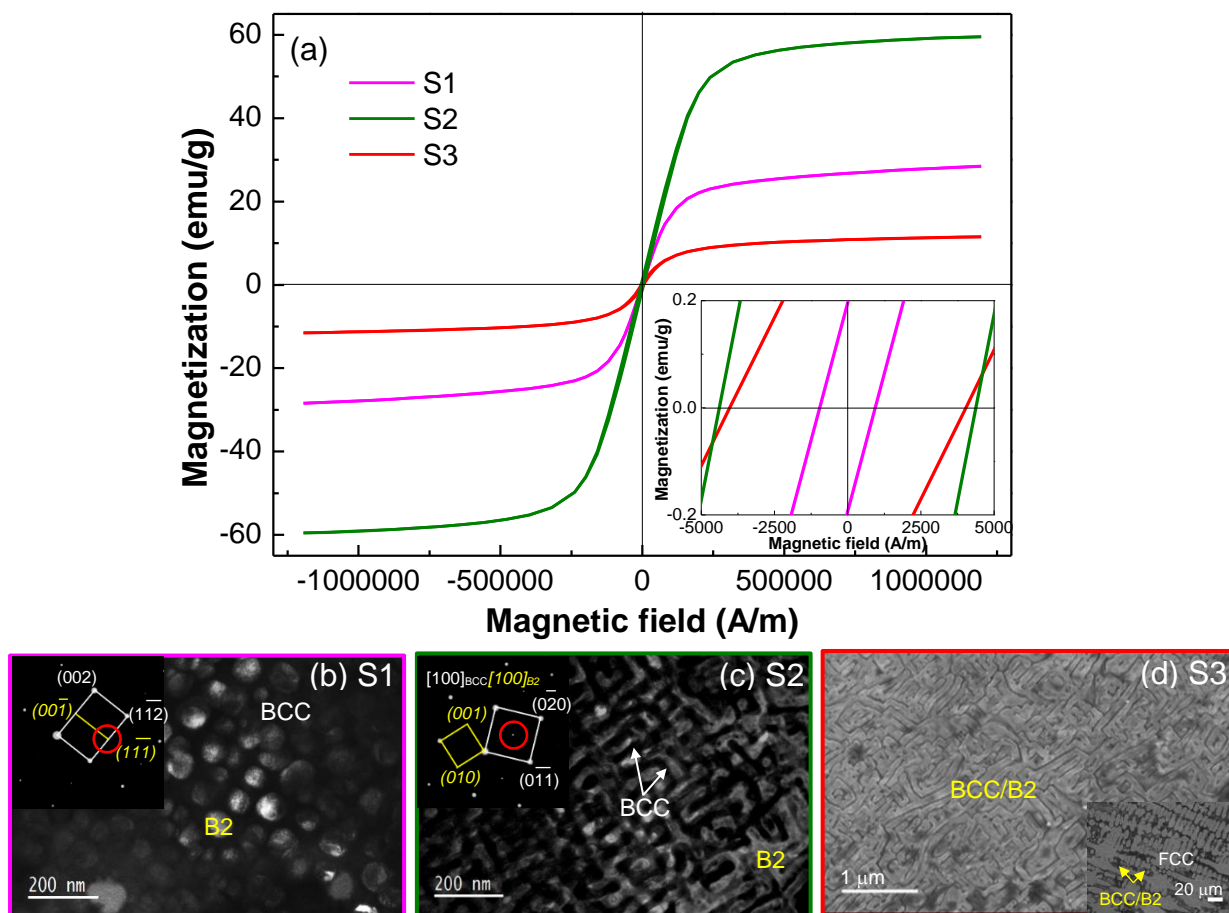
Figure S6. (a) Hysteresis loops of S1-S3 HEAs. TEM dark-field (DF) images and the corresponding selected-area electron diffraction (SAED) patterns of S1 and S2 alloys, as well as the OM and SEM images of S3 alloy are shown in (b), (c) and (d), respectively.

Table S1. Magnetic properties of the current $Al_{1.5}Co_4Fe_2Cr$ ($Al_{17.65}Co_{47.06}Fe_{23.53}Cr_{11.76}$, at. %) alloy heat-treated at different temperatures, including the saturation magnetization (M_S), saturation induction intension (B_S), and coercivity (H_C).

	Treatment	M_S (emu/g)	B_S [a] (T)	H_C (Oe)	H_C (A/m)
A-773	1573K/2h+773K/24h	135.3	1.3	1.6	127.3
A-873	1573K /2h+873K/24h	128.5	1.2	1.4	111.4
A-973	1573K /2h+973K/24h	103.5	1.0	67.6	5379.4
A-1073	1573K /2h+1073K/24h	49.5	0.5	59.7	4750.8
8 h	1573K /2h+773K/24h +873K/8h	130.9	1.2	1.4	111.4
70 h	1573K /2h+773K/24h +873K/70h	130.9	1.2	2.1	167.1
305 h	1573K /2h+773K/24h +873K/305h	126.3	1.2	2.1	167.1
555 h	1573K /2h+773K/24h +873K/555h	126.1	1.2	2.7	214.9

[a] $B_S = 4\pi \cdot M_S \cdot \rho_m / 10000$, in which $\rho_m = 7.36$ g/cm^3 is the mass density of $Al_{1.5}Co_4Fe_2Cr$ alloy.

Table S2. Data summary of other Al-Ni-Co-Fe-Cr HEAs, including the alloy composition (at. %), phase constitutions, mass density (ρ_m), saturation magnetization (M_S), saturation induction intension (B_S), and coercivity (H_C).

	Alloy composition (at. %)	Phase constitution	ρ_m (g/cm^3)	M_S (emu/g)	B_S [a] (T)	H_C (Oe)	H_C (A/m)
S1-Al$_{0.7}$NiCoFeCr$_2$	Al$_{12.5}$Ni$_{17.5}$Co$_{17.5}$Fe$_{17.5}$Cr$_{35}$	BCC+B2 particles	7.35	28.9	0.3	11.9	947.0
S2-Al$_{0.86}$NiCoFeCr	Al$_{17.65}$Ni$_{20.59}$Co$_{20.59}$Fe$_{20.59}$Cr$_{20.59}$	BCC+B2 (weave-like)	7.24	59.6	0.5	55.0	4376.8
S3-Al$_{0.57}$NiCoFeCr	Al$_{12.5}$Ni$_{21.88}$Co$_{21.88}$Fe$_{21.88}$Cr$_{21.88}$	FCC+BCC/B2 (weave-like)	7.53	11.7	0.1	50.7	4034.6

[a] $B_S = 4\pi \cdot M_S \cdot \rho_m / 10000$.

Table S3. Alloy composition (at. %), saturation induction intension (B_S), the mean magnetic moment per atom ($\overline{\mu}_H$), and the ratio of $P = B_s/\overline{\mu}_H$ of typically existing soft-magnetic alloys and the current $Al_{1.5}Co_4Fe_2Cr$ alloy.

	Alloy composition (at. %)	Bs (T)	$\overline{\mu}_H$ (μ_B)	P
$Al_{1.5}Co_4Fe_2Cr$	$Al_{17.65}Co_{47.06}Fe_{23.53}Cr_{11.76}$	1.3	1.32	0.98
S1	$Al_{12.5}Ni_{17.5}Co_{17.5}Fe_{17.5}Cr_{35}$	0.3	0.79	0.34
S2	$Al_{17.65}Ni_{20.59}Co_{20.59}Fe_{20.59}Cr_{20.59}$	0.5	0.93	0.59
S3	$Al_{12.5}Ni_{21.88}Co_{21.88}Fe_{21.88}Cr_{21.88}$	0.1	0.98	0.11
Finmet alloy [8]	$Fe_{73.5}Si_{13.5}B_9Cu_1Nb_3$	1.2	1.62	0.74
Nanoperm alloy [28]	$Fe_{91}Zr_7B_2$	1.7	2.00	0.85
Hitperm alloy [6,7]	$Fe_{44}Co_{44}Zr_7B_4Cu_1$	2.0	1.72	1.17
FeCoNi(AlSi)$_{0.1}$ [16]	$Fe_{32.26}Co_{32.26}Ni_{32.26}Al_{1.61}Si_{1.61}$	1.3	1.45	0.90
FeCoNi(AlSi)$_{0.2}$ [16]	$Fe_{31.25}Co_{31.25}Ni_{31.25}Al_{3.13}Si_{3.13}$	1.1	1.41	0.78
$Al_{0.5}FeCoNi$ [17]	$Al_{14.29}Fe_{28.57}Co_{28.57}Ni_{28.57}$	0.99	1.29	0.77
$Al_{0.75}FeCoNi$ [17]	$Al_{20}Fe_{26.67}Co_{26.67}Ni_{26.67}$	0.98	1.20	0.82
AlFeCoNi [17]	$Al_{25}Fe_{25}Co_{25}Ni_{25}$	0.85	1.13	0.75
$Al_{0.25}FeCoNiMn_{0.25}$ [29]	$Al_{7.14}Fe_{28.57}Co_{28.57}Ni_{28.57}Mn_{7.14}$	1.0	1.29	0.78

Table S4. Alloy composition (at. %), room-temperature electrical resistivity (ρ) and Curie temperature (T_C) of the typically existing typical soft-magnetic alloys and the current $Al_{1.5}Co_4Fe_2Cr$ alloy.

	Alloy composition (at. %)	ρ ($\mu\Omega\cdot$cm)	T_C (K)
$Al_{1.5}Co_4Fe_2Cr$	$Al_{17.65}Co_{47.06}Fe_{23.53}Cr_{11.76}$	244	1061
Fe [9,31]	Fe	10	1043
3Si-Fe [9,31]	$Si_{5.79}Fe_{94.21}$	45	1013
6.5Si-Fe [9,31]	$Si_{12.14}Fe_{87.86}$	82	973
50Ni-Fe [9,31]	$Ni_{48.76}Fe_{51.24}$	54	773
79Ni-5Mo-Fe [9,31]	$Ni_{79.9}Mo_{3.09}Fe_{17.01}$	60	673
50Co-2V-Fe [9,31]	$Co_{48.56}V_{2.25}Fe_{49.19}$	40	1253
Hitperm alloy [6,7]	$Fe_{44}Co_{44}Zr_7B_4Cu_1$	150	1253
$Fe_{78}Si_9B_{13}$ [32]	$Fe_{78}Si_9B_{13}$	137	961
$Fe_{40}Ni_{40}P_{14}B_6$ [32]	$Fe_{40}Ni_{40}P_{14}B_6$	180	796
$Al_{0.25}FeCoNiMn_{0.25}$ [30]	$Al_{7.14}Fe_{28.57}Co_{28.57}Ni_{28.57}Mn_{7.14}$	100	1078

References

[S1] W. F. Hosford, *Mechanical behavior of materials*, Cambridge University Press, New York, USA **2005**.

[S2] D. B. Cullity, S. R. Stock, *Elements of X-Ray Diffraction*, Prentice Hall, New Jersey, USA **2011**.

[S3] K. Thompson, D. Lawrence, D.J. Larson, J. D. Olson, T. F. Kelly, B. Gorman, *Ultramicroscopy* **2007**, *107*, 131.

[S4] B. Gault, M. Moody, F. D. Geuser, G. Tsafnat, A. L. Fontaine, L. Stephenson, D. Haley, S. Ringer, *J. Appl. Phys.* **2009**, *105*, 772.

[S5] C. A. Schneider, W. S. Rasband, K. W. Eliceiri, *Nat. Methods* **2012**, *9*, 671.

[S6] B. D. Cullity, C. D. *Graham, Introduction to magnetic materials*, Addison Wesley, Boston, USA **1972**.

[S7] C. Dong, Q. Wang, J. B. Qiang, Y. M. Wang, N. Jiang, G. Han, Y. H. Li, J. Wu, J. H. Xia, *J. Phys. D: Appl. Phys*. **2007**, *40*, R273.

[S8] C. Pang, B. B. Jiang, Y. Shi, Q. Wang, C. Dong, *J. Alloy. Compd.* **2015**, *652*, 63.

[S9] Z. R. Wang, J. B. Qiang, Y. M. Wang, Q. Wang, D. D. Dong, C. Dong, *Acta Mater*. **2016**, *111*, 366.

[S10] Y. Ma, Q. Wang, C. L. Li, L. J. Santodonato, M. Feygenson, C. Dong, P. K. Liaw, *Scripta Mater.* **2018,** *144*, 64.

[S11] I. Mirebeau, M. Hennion, G. Parette, *Phys. Rev. Lett.* **1984**, *53*, 687.

[S12] J. M. Cowley, *Phys. Rev.* **1950**, *77*, 669.

[S13] P. Singh, A. V. Smirnov, D. D. Johnson, *Phys. Rev. B* **2015**, *91,* 224204.

[S14] R. C. Brouwer, R. Griessen, *Phys. Rev. B* **1989**, *40*, 1481.

[S15] H. W. Sheng, W. K. Luo, F. M. Alamgir, J. M. Bai, E. Ma, *Nature* **2006**, *439*, 419.

[S16] A. Takeuchi, A. Inoue, *Mater. Trans*. **2005**, *46*, 2817.

[S17] W. Guo, W. Dmowski, J. Y. Noh, P. Rack, P. K. Liaw, T. Egami, *Metall. Mater. Trans. A* **2013**, *44*, 1994.

[S18] M. C. Gao, D. E. Alman, *Entropy* **2013**, *15*, 4504.

[S19] Y. Ma, Q. Wang, B. B. Jiang, C. L. Li, J. M. Hao, X. N. Li, C. Dong, T. G. Nieh, *Acta Mater*. **2018,** *147*, 213.

[S20] Y. Ma, J. M. Hao, Q. Wang, C. Zhang, C. L. Li, C. Dong, *J. Mater. Sci*. **2019**, *54*, 8696.

[S21] G. Herzer, in *Handbook of magnetic materials*, Vol. 10 (Ed: K. H. J. Buschow), Elsevier Science BV, Amsterdam, the Netherlands, **1997**.

[S22] W. D. Zhong, *Ferro magnetics*, Science Press, Beijing, China **1987**.

[S23] F. E. Luborsky, J. D. Livingston, G. Y. CHIN, in *Physical Metallurgy*, Vol. 3 (Eds: R. W. Cahn, P. Haasen), Elsevier Science BV, Amsterdam, the Netherlands, **1996**, Ch. 29.

[S24] S. Huang, W. Li, X. Q. Li, S. Schönecker, L. Bergqvist, E. Holmström, L. K. Varga, L. Vitos, *Mater. Des*. **2016**, *103*, 71.

[S25] L. J. Santodonato, Y. Zhang, M. Feygenson, C. M. Parish, M. C. Gao, R. J. Weber, J. C. Neuefeind, Z. Tang, P. K. Liaw, *Nat. Commun*. **2015**, *6*, 5964.

[S26] Y. P. Wang, B. S. Li, M. X. Ren, C. Yang, H. Z. Fu, *Mater Sci. Eng. A* **2008**, *491*, 154.

[S27] Y. F. Kao, T. J. Chen, S. K. Chen, J. W. Yeh, *J. Alloys Compd.* **2009**, *488*, 57.

[S28] Y. Ma, B. B. Jiang, C. L. Li, Q. Wang, C. Dong, P. K. Liaw, F. Xu, L. Sun, *Metals* **2017**, *7*, 57.

[S29] C. L. Li, Y. Ma, J. M. Hao, Y. Yan, Q. Wang, C. Dong, P. K. Liaw, *Mater. Sci. Eng. A* **2018**, *737*, 286.

[S30] O. N. Senkov, S. V. Senkova, C. Woodward, *Acta Mater*. **2014**, *68*, 214.

[S31] S. Z. Niu, H. C. Kou, T. Guo, Y. Zhang, J. Wang, J. S. Li, *Mater. Sci. Eng. A* **2016**, *671*, 82.

[S32] P. W. Voorhees, G. B. Mcfadden, W. C. Johnson, *Acta Metall. Mater*. **1992**, *40*, 2979.

[S33] P. Fratzl, O. Penrose, J. L. Lebowitz, *J. Stat. Phy.* **1999**, *95*, 1429.

[S34] M. E. Thompson, C. S. Su, P. W. Voorhees, *Acta Metall. Mater*. **1994**, *42*, 2107.

[S35] E. A. Marquis, D. N. Seidman, *Acta Mater*. **2011**, *49*, 1909.

[S36] P. Villars, L. D. Calvert, *Pearson's Handbook of Crystallographic Data for Intermetallic Phases*, ASM, Metals Park OH, USA **1985**.

[S37] C. Radeloff, I. Pfeiffer, *IEEE Transactions on Magnetics* **1975**, *11*, 1417.